*Acta Cryst.* (1984). A40, 143–151

# Lattice-Image Interpretation of a Relatively-Small-Unit-Cell Crystal

BY MINORU TANAKA AND BERNARD JOUFFREY

*Laboratoire d'Optique Electronique du CNRS, Laboratoire Propre du CNRS associé à l'Université Paul Sabatier, 29, rue Jeanne Marvig, BP* 4347, 31055 *Toulouse CEDEX, France*

(*Received* 24 *January* 1983; *accepted* 8 *November* 1983)

## Abstract

Many-beam lattice images obtained at 200 kV from $V_2O_3$ crystals are discussed in comparison with those calculated in the Bloch-wave approach. The technique of optical diffractogram and equal-thickness fringes is utilized, if possible, to determine the defocus value and the crystal thickness which are the essential parameters for objective interpretation at atomic resolution. Whereas images observed in a thin region ($\lesssim$50 Å) of crystal have been reproduced fairly well by simulation, there are others from thicker regions which are not always explained for lack of knowledge of the parameters. As for the effect of the partial coherence, the validity of the envelope-function approximation is examined with the aid of the first principle involving image-intensity summation, and under the experimental conditions used it proved to be satisfactory for qualitatively reproducing the observed image even for relatively thick ($\lesssim$450 Å) regions.

## 1. Introduction

Since the first structure image was obtained from a complex oxide crystal $Ti_2Nb_{10}O_{29}$ (Iijima, 1971), the lattice-imaging technique in zone-axis orientation is more and more used in different fields to study a variety of crystal structures. In the case of large-unit-cell crystals where the Scherzer defocus (Scherzer, 1949) is the optimum condition, this is detectable on the observation screen by varying the objective-lens excitation current to search for an image resembling a projection of the crystal structure known through an X-ray technique. One can then conceive a model structure for crystal defects, if there are any in the image thus obtained, and test it on the computer (for example, see O'Keefe & Iijima, 1978). On the contrary, when a crystal of relatively small unit cell ($\lesssim$5 Å) is to be studied or when it is no longer atom groups but atoms themselves (always projected columns of atoms) that have to be visualized, it is not always the Scherzer condition that will furnish an image with as much directly usable information as possible, partly because of the limited performance of the microscope and partly because of the failure of the weak-phase-object approximation for a crystal of practical thickness (Tanaka & Jouffrey, 1980). Then the presence of one-to-one correspondence at atomic resolution cannot be predicted by a simple theory (Cowley & Iijima, 1972) between the real crystal structure and an image bearing details of the order of 1 Å, thus necessitating the interpretation of observed images with the aid of image simulation.

In practice, when the resolution required by the object is of the order of interatomic distances and so is near or superior to the limit of the resolution of a microscope, the difficulty is doubled: under what observation conditions (especially the defocus value and the crystal thickness) does the resulting image bear as much usable information as possible, and how can we know if these conditions are really satisfied on the microscope? In fact, there are some anomalies encountered in analyzing lattice images obtained from perfect crystals (Spence, O'Keefe & Kolar, 1977; Bursill, 1978–79; Hashimoto, Endoh, Takai, Tomioka & Yokota, 1978–79; Krakow, 1979; Krivanek & Rez, 1980; Ishizuka & Iijima, 1981). A more complete comprehension of the lattice image from 'perfect' crystals appears to be necessary so that the technique may become a really powerful tool for studying unknown crystal defects or a localized structure in an object at atomic resolution.

Through the progress accomplished in the performance of the microscope one can work, apart from the case of high-voltage machines, under experimental conditions such that the effect of the partial coherence may not be very important, though this depends on the defocus value. Nevertheless, it cannot be negligible at present in the lattice-image interpretation. Here, there is also a problem with the envelope-function approximation (Frank, 1973; Fejes, 1977) currently used in order to allow for the partial coherence, because of the underlying assumption of the weak object. The higher the required resolution, the stronger is the interaction between the electron and the object since electrons scattered at larger angles are needed to form the image.

In this paper we describe an interpretation of lattice images obtained from the vanadium sesquioxide ($V_2O_3$) crystal at the accelerating voltage of 200 kV.

Also, the validity of the envelope-function approximation is examined under the experimental conditions used. The stress is placed on the importance of knowing the two parameters, defocus value and crystal thickness, to interpret objectively the lattice image of a crystal having a relatively small unit cell. The interest of using a $V_2O_3$ crystal as test object is that its unit cell has a structure which is neither so simple as, for example, f.c.c. crystals, nor so complex as large-unit-cell oxide crystals; the image contrast at atomic resolution can therefore be studied. We note in passing that the crystal shows a metal–semiconductor phase transition at about 150 K, which has also been observed in electron microscopy (Launay, Pouchard, Ayroles & Jouffrey, 1975).

## 2. Experimental

High-quality $V_2O_3$ single crystals grown by the gas-transport technique were kindly provided by Dr Launay (1977). They were ground in a hard-glass tube and the powder thus obtained was deposited on a glow-discharge-treated microgrid of polycrystalline gold, without any liquid suspension. The preparation was examined in a JEOL-200CX electron microscope equipped with a top-entry-type goniometer stage of inclination limited to about 11° and with a thermal-emission pointed filament. The emission current was 5 μA or lower.

Fig. 1 shows the representative electron diffraction patterns of the high-temperature metallic-phase vanadium sesquioxide $V_2O_3$. The space group is $R\bar{3}c$ and the two-molecule rhombohedral cell has the parameters $a_R = 5{\cdot}473$ Å and $\alpha = 53{\cdot}79°$. The presence, in the selected area, of a part of the holey polycrystalline-gold support gives rise to the ring pattern which serves not only to index unambiguously the recorded diffraction pattern of $V_2O_3$, but also to recognize immediately each spot pattern on the observation screen in the microscope. The diffraction patterns (*a*), (*b*), (*c*) and (*d*) belong to the zone axes $[2\bar{2}1]$, [211], [010] and [001] in the hexagonal-system indexation. The first three correspond respectively to the base vectors $a_M$, $c_M$, $b_M$ of the monoclinic cell which characterizes $V_2O_3$ in the low-temperature phase (<150 K), while the fourth is obviously parallel to $c_H$. The diffraction pattern (*e*) is that of the zone axis $[\bar{4}11]$. Exploitable lattice images have been obtained in the three orientations (*a*), (*c*) and (*e*). Fig. 1(*f*) shows, on the $[\bar{4}11]$ pattern, the size of the objective aperture and that of the second-condensor-lens aperture used in lattice imaging with the incident electron beam focused on the specimen. The axial illumination was used throughout the experiments with the centered objective aperture of radius $R = 0{\cdot}94$ Å$^{-1}$. The second-condensor aperture defines an effective source (Frank, 1973) of radius $u_s = 0{\cdot}030$ Å$^{-1}$. Kodak electron-image films of type 4463 were used to record the image. The exposure time was 8 s at the nominal magnification of $550 \times 10^3$. The spherical aberration constant was measured on the amorphous contamination formed on the crystal during observation. The method proposed by Krivanek (1976) was used in combination with the least-squares regression analysis (Tanaka & Jouffrey, 1981) and gave $C_s$ values around 1·0 mm.

Positive prints were produced directly (one step) from original negatives by the standard photographic treatment; no kind of image processing for contrast enhancement was used.

## 3. Lattice-image calculations

Using the Bloch-wave formulation of electron diffraction we have developed a program (Tanaka & Jouffrey, 1980) to calculate many-beam lattice images. The absorption effect due to phonon scattering is allowed for as the first-order perturbation (Hirsch, Howie, Nicholson, Pashley & Whelan, 1965). All the Fourier coefficients of the imaginary potential were calculated by treating each Bloch wave independently of the others (Hall & Hirsch, 1965; Radi, 1970), but the mean absorption potential used is that measured at 100 kV and corrected for 200 kV, namely 0·54 V. The Debye temperature of the $V_2O_3$ crystal was taken to be 630 K (Andrianov & Drichko, 1976). Once the eigenvalues, the eigenvectors and the absorption coefficients have been calculated for a particular excitation condition of symmetric incidence they are stored on magnetic tape and can thus be exploited to simulate lattice images corresponding to various combinations of parameters such as the crystal thickness, defocus value, effective source size, defocus spread, *etc.* The number of waves used in the calculation of the wave field on the crystal exit surface is 87 for $[2\bar{2}1]$ and [010] orientations, and 65 waves for the $[\bar{4}11]$ orientation. In the latter case some calculations were done with 101 waves, but differences between the images corresponding to 65 and 101 waves were virtually indiscernible even for a thick crystal (700–800 Å). As for the effect of the partial coherence on the image contrast, the program offers an option between the intensity-sum method (see § 4) and the envelope-function approximation. In the latter the coupling between the spatial and temporal coherences was ignored because it is negligible when the generalized 'cross-term parameter' $A = 2(\pi u_s \sigma)^2 (\lambda / C_s)^{1/2}$ is smaller than 0·0138 (Wade & Frank, 1977), as is the case for our experiments. Unless mentioned otherwise, the partial coherence is taken into account in the image simulation by using the envelope function where a disk-shaped source of radius $u_s = 0{\cdot}030$ Å$^{-1}$ (measured) and a Gaussian distribution of standard deviation $\sigma = 50$ Å (Olsen & Spence, 1981) for defocus spread were assumed.

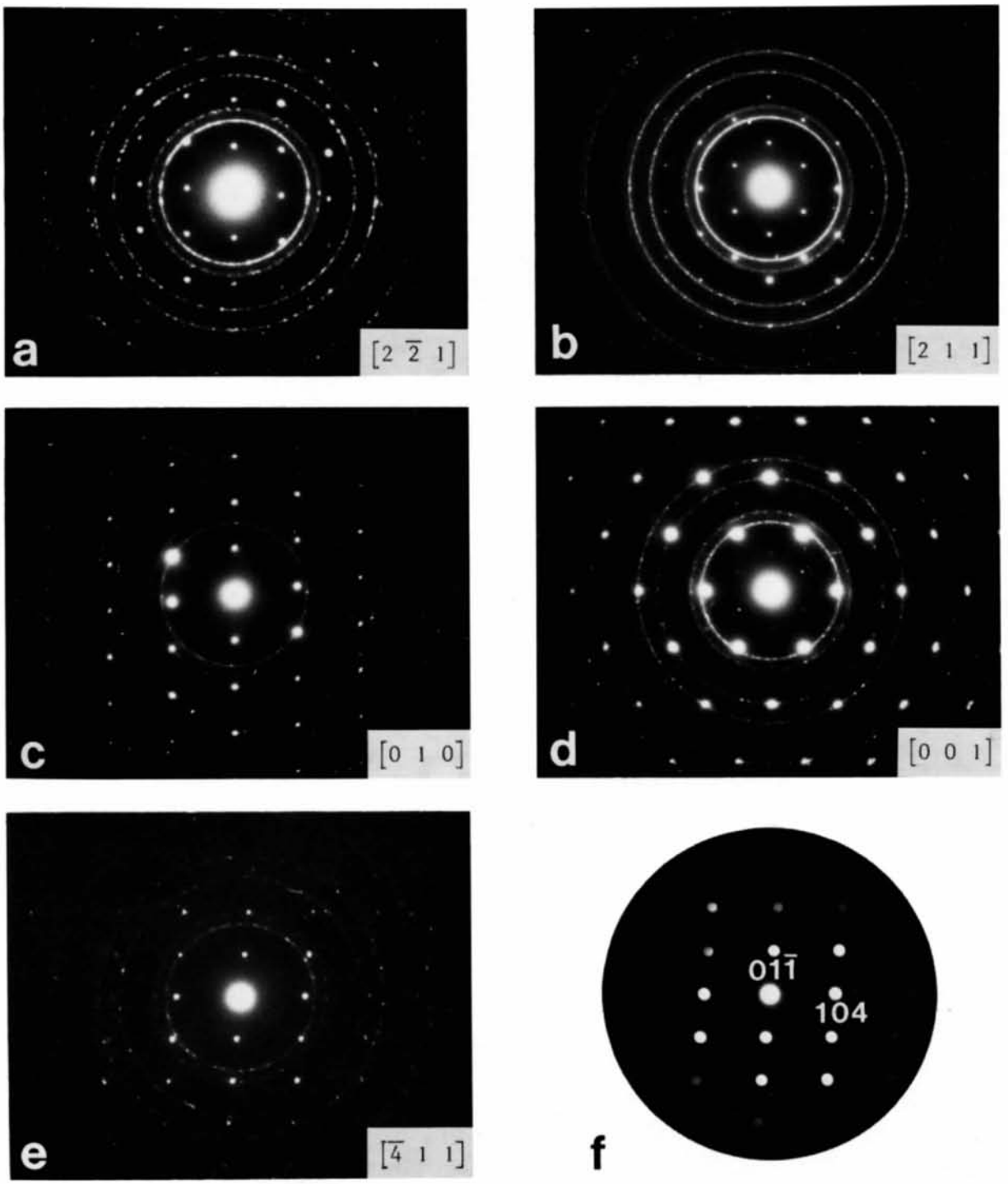


Fig. 1. Representative electron diffraction patterns of high-temperature phase $V_2O_3$ crystals supported on the polycrystalline gold microgrid. Zone axes in hexagonal-system indexes are (*a*) [2$\bar{2}$1], (*b*) [211], (*c*) [010], (*d*) [001] and (*e*) [$\bar{4}$11]. The diffraction pattern (*f*), also of [$\bar{4}$11], shows the size of the second-condensor-lens and the objective-lens apertures used in lattice imaging.

[*To face p. 144*

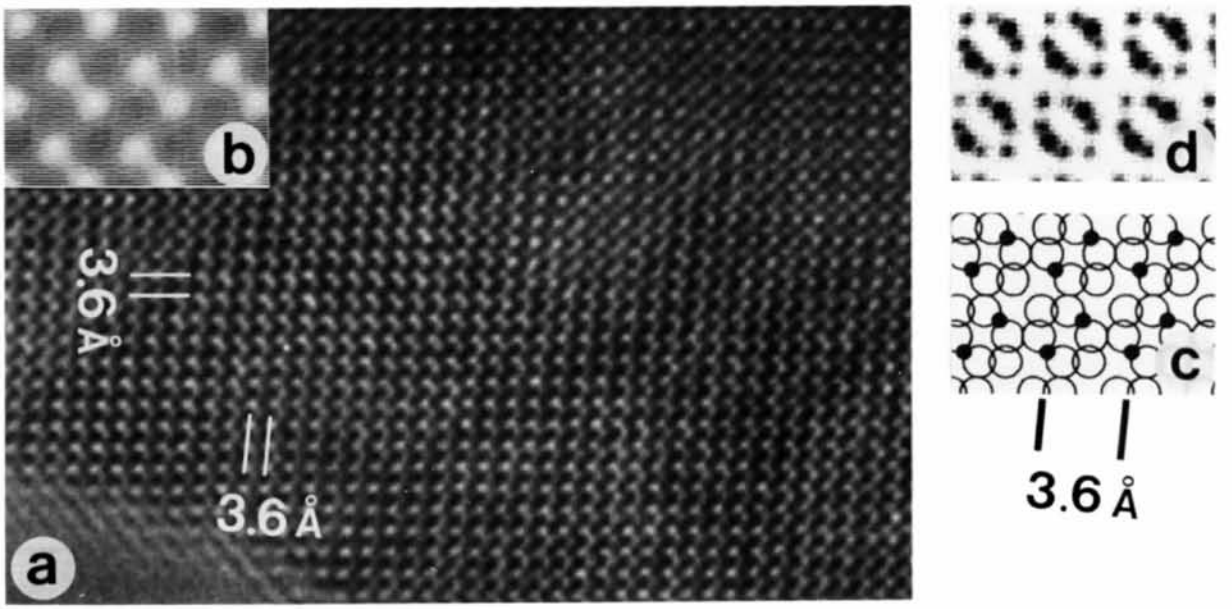


Fig. 2. [$2\bar{2}1$] lattice image (*a*) with the corresponding simulated image (*b*) at the crystal thickness $z = 50$ Å and the defocus value $\Delta f = 550$ Å. (*c*) Projected structure: dots and circles designate columns of vanadium and oxygen atoms, respectively. (*d*) Projected potential distribution: the dark part corresponds to a higher-potential area. The nearest-neighbour columns (separated by 2·1 Å) of vanadium atoms are not resolved and are situated in the dark area in the image (*a*).

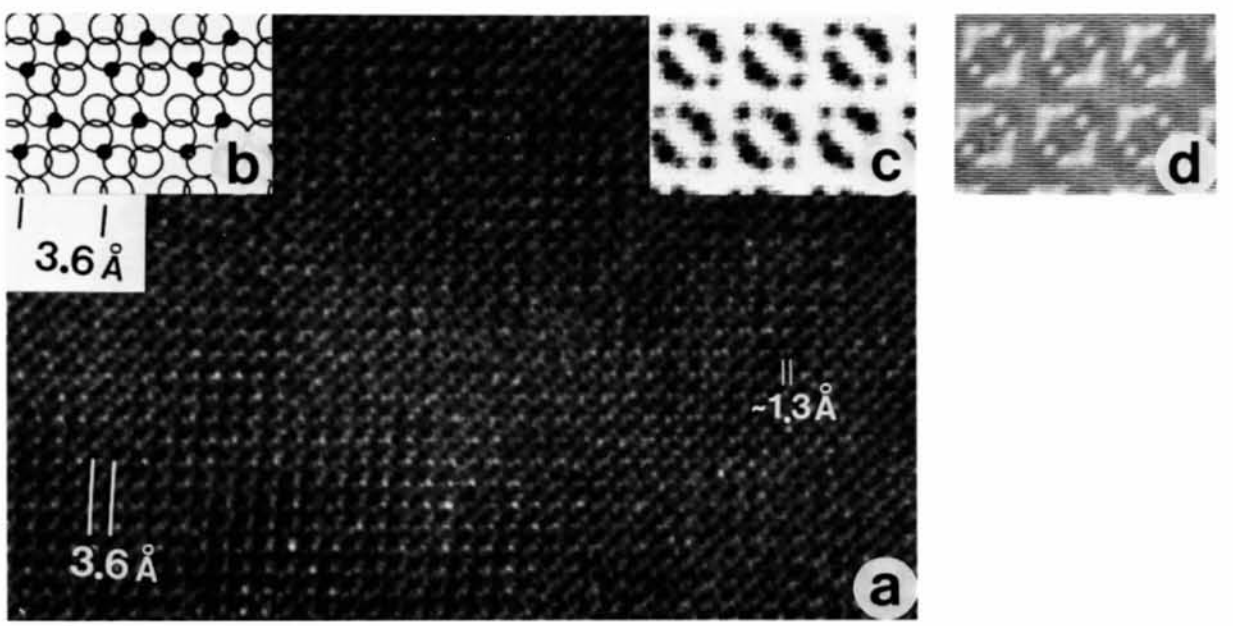


Fig. 4. (*a*) [$2\bar{2}1$] lattice image. The image appearance in the central region bears some resemblance to the projected potential distribution (*c*) with inverse contrast. (*b*) Projected structure. (*d*) A simulation at $z = 100$ Å and $\Delta f = 450$ Å in the perfectly coherent case. This type of calculated image appearance is completely destroyed when the partial coherence is taken into consideration. Note that there are several pairs of small bright dots separated by $\leq 1{\cdot}3$ Å visible in the image (*a*).

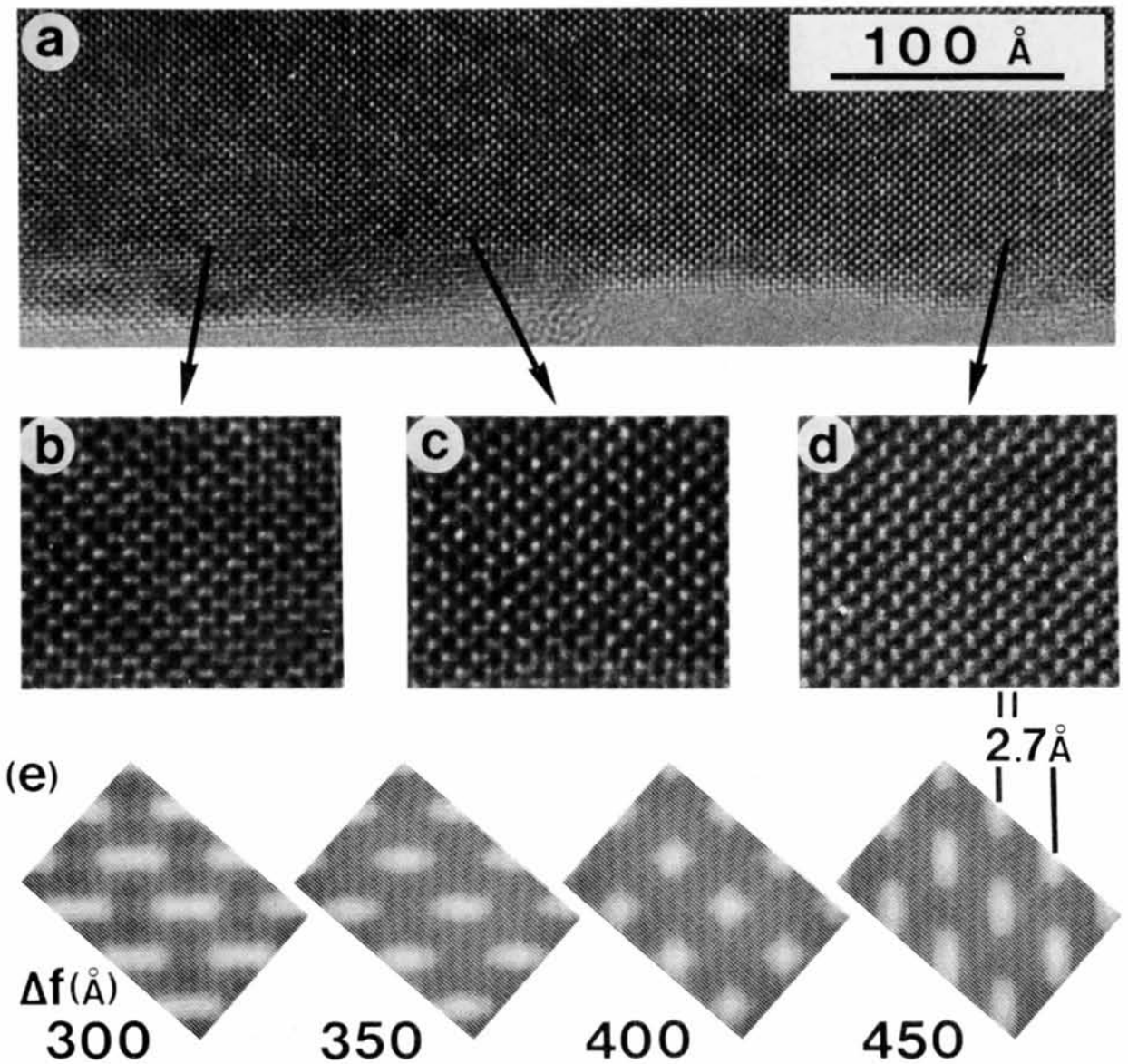


Fig. 3. (*a*) [$2\bar{2}1$] lattice image showing a variation of image appearance due to an inclined crystal edge, (*b*)–(*d*) enlarged micrographs from three regions in (*a*), and (*e*) simulated images at $z = 50$ Å.

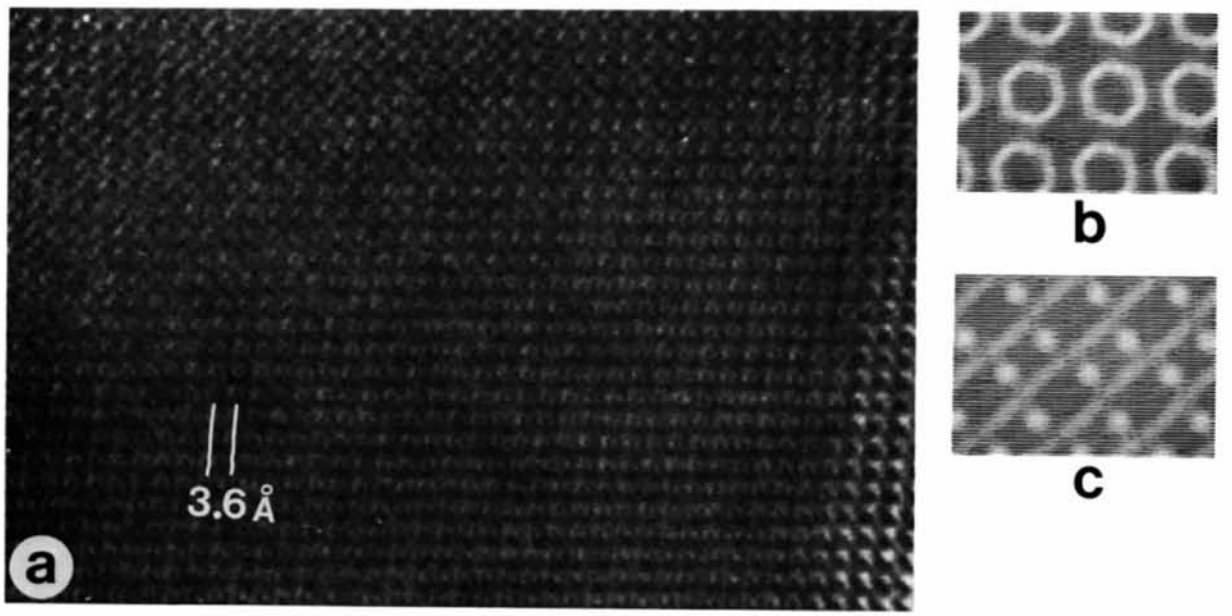


Fig. 5. (*a*) [2$\bar{2}$1] lattice image where the crystal thickness increases from lower right corner to upper left. In the intermediate region, an array of small white circles having a diameter of *ca* 1·7 Å is visible. (*b*) A simulation at $z = 100$ Å and $\Delta f = 1350$ Å in the perfectly coherent case. (*c*) A simulation ($z$, $\Delta f$ the same as above) with the finite partial coherence allowed for by the intensity-sum method (see text) taking $u_s = 0{\cdot}030$ Å$^{-1}$ and $\sigma = 50$ Å.

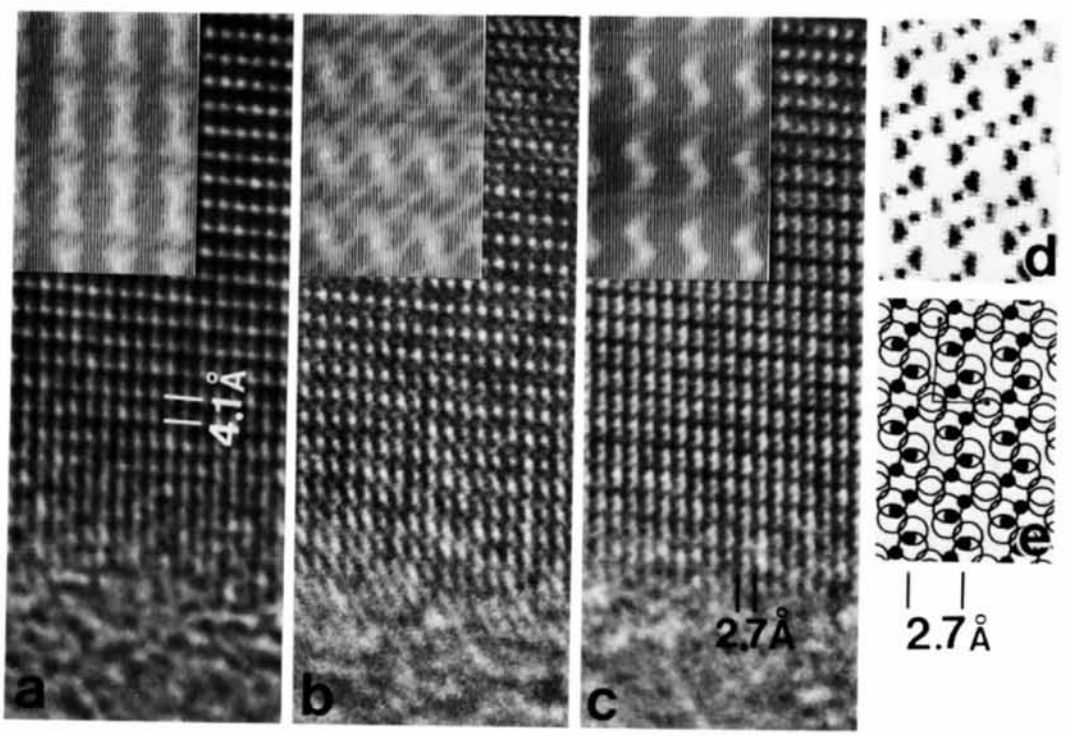


Fig. 9. [$\bar{4}$11] lattice images from which resulted the optical diffractograms shown in Fig. 8. The insets are the best-matched simulations made at $z = 50$ Å and (*a*) $\Delta f = 650$ Å, (*b*) 1000 Å and (*c*) 1150 Å. The temporal coherence is taken into account by use of the intensity-sum method. (*d*) Projected potential distribution. (*e*) Projected structure with the same conventions as in Fig. 2.

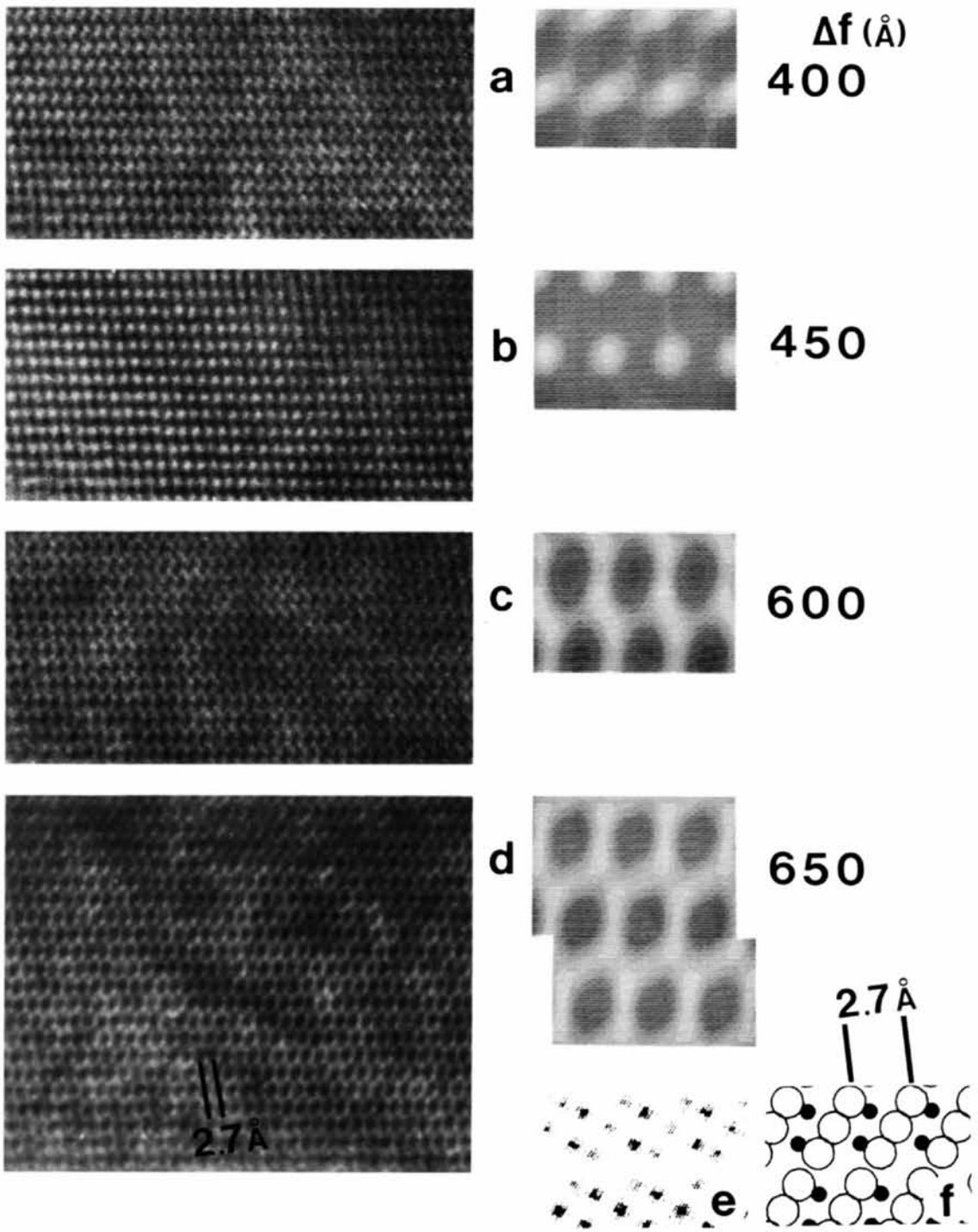


Fig. 6. [010] lattice images. (*a*)–(*d*) Part of focus series with the corresponding simulations at $z = 50$ Å. (*e*) Projected potential distribution and (*f*) projected structure with the same convention as in Fig. 2.

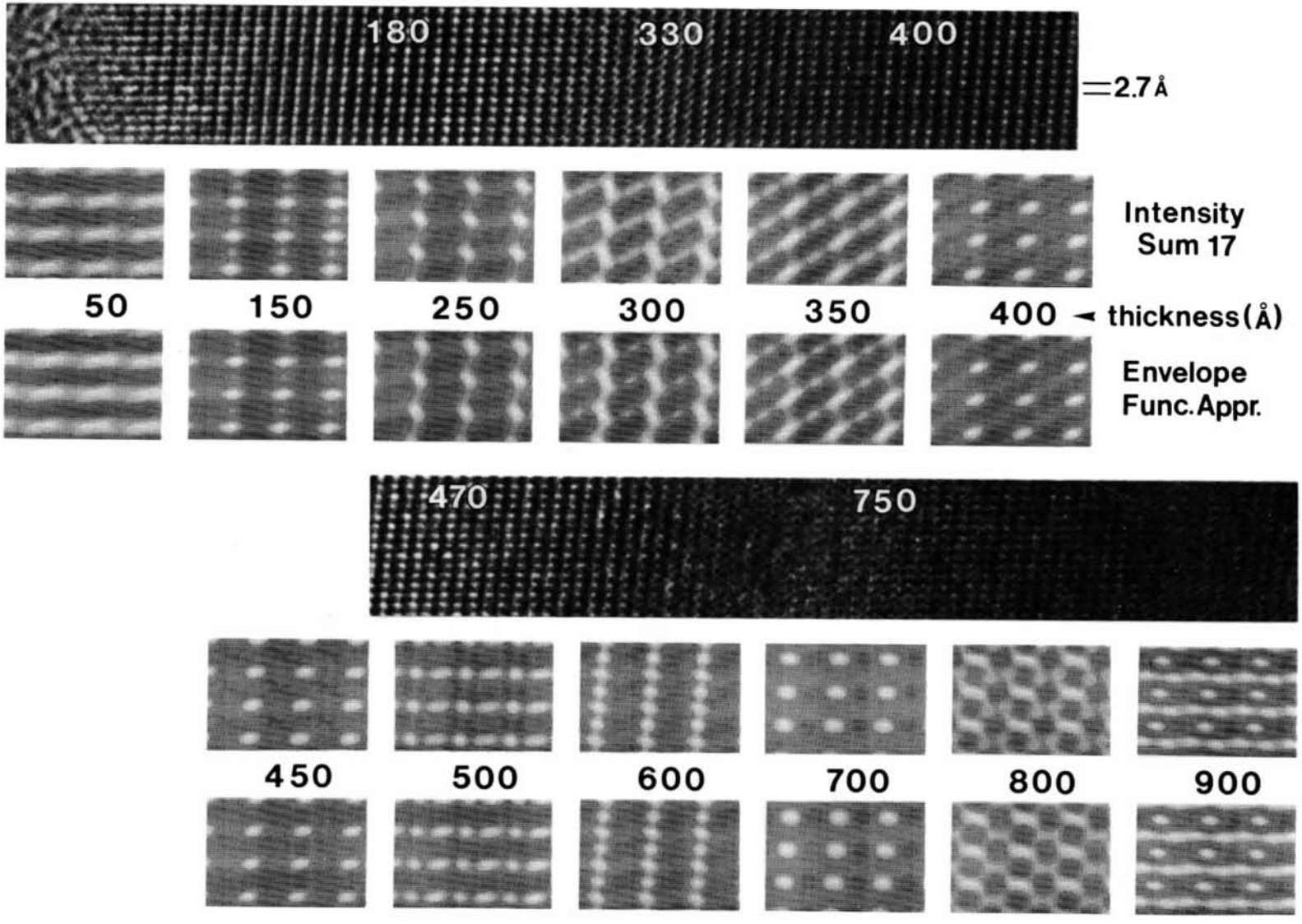


Fig. 12. [$\bar{4}11$] lattice image of a wedge-shaped crystal. The crystal thickness indicated on the experimental image is estimated from the profile of the equal-thickness fringes shown in Fig. 7. Image simulations were carried out using two different ways of taking into account the partial coherence: intensity sum 17 refers to that which consists of summing image intensities calculated for the 17 directions (shown in Fig. 11) using the reduced objective aperature of $R = 0{\cdot}77$ Å$^{-1}$, and the other is the envelope-function approximation which was applied with a disk-shaped source of radius $u_s = 0{\cdot}030$ Å$^{-1}$, the defocus spread $\sigma = 50$ Å, and the actual objective aperture $R = 0{\cdot}94$ Å$^{-1}$. The crystal thicknesses used in simulations are indicated, each between the two corresponding images.

## 4. Results and discussion

### 4.1. *Interpretation of lattice images*

One of the images obtained in a thin region of a crystal oriented along the [2$\bar{2}$1] zone axis is reproduced in Fig. 2(*a*). The inset (*b*) is an image calculated at the crystal thickness $z = 50$ Å and the defocus value $\Delta f = 550$ Å.* The simulation also shows very similar but translated images around $\Delta f = 1025$ Å. However, this is not plausible because of the focus setting used. Fig. 2(*c*) shows atom positions viewed along the zone axis: dots and circles designate respectively columns of vanadium atoms and oxygen atoms. Since the electron scattering is due to the electrostatic potential of the object, it is useful to know the distribution of the crystal potential encountered by the incident electrons. For this reason a program independent of the lattice-image simulation was written to calculate the projected potential of a crystal. The method used here is that of the real space: calculate the projected potential of a single atom by assuming the Wentzel–Yukawa model for each atom species with the Thomas–Fermi radius, and then distribute the potential thus obtained to projected atom positions of corresponding species taking account of the number of superpositions for a given crystal thickness. Because of the model used to simplify the potential calculation the resulting projected-potential distribution is not precise, but it is sufficient for the use of qualitative comparison of the potential between different atomic columns. The projected potential calculated in this way is shown in Fig. 2(*d*), where the region of higher potential appears darker. Fig. 2(*c*), (*d*) and the simulated image cover the same area of crystal at the same magnification. Therefore, the simulated image serves as a bridge between the observed one and the projected structure of the crystal.

It is seen that this type of image, having a peanut-like appearance, does not directly reflect the crystal structure, and that the nearest-neighbour columns of vanadium atoms (separated by 2·09 Å) are unresolved and situated at the dark part in the observed image. This is the same type of image as that predicted at 100 kV for a thin crystal (Fig. 4*b* in Tanaka & Jouffrey, 1980). However, the focus condition was $Z = \Delta f/(C_s\lambda)^{1/2} = 2{\cdot}3$ there, while $Z = 1{\cdot}1$ in the present case. It is because of the differences in $C_s$ and $\lambda$ that the transfer conditions for the three lowest spatial frequencies (1/3·66, 1/2·71 and 1/2·48 Å$^{-1}$) are nearly the same for these different focus conditions.

Fig. 3 shows an image (*a*) obtained from a thin part of another crystal in the [2$\bar{2}$1] orientation, where a variation of image appearance occurs along the edge of the crystal as is seen in the enlarged micrographs (*b*, *c*, *d*) from three regions. In fact, the image simulation (*e*) shows that a difference of about 100 Å in defocus value is sufficient to give rise to such a variation of image; that is, horizontally elongated white patches on the left (*b*) become vertical on the right-hand side (*d*) after passing simple dots in between (*c*). Since there is no fourfold axis parallel to [2$\bar{2}$1], these two types of images (*b*) and (*d*) can be distinguished from each other. According to the defocus values of the simulated images, therefore, the edge of the crystal is not in a plane perpendicular to the optical axis but inclined down towards the right. The crystal thickness was taken to be 50 Å in the simulation.

The following two images were also obtained in the [2$\bar{2}$1] orientation but far from the edge and so from thick (probably $z \gtrsim 100$ Å) regions of crystals. The central part of the image reproduced in Fig. 4(*a*) has some resemblance to the projected potential (*c*) with reversed contrast, while the image in Fig. 5(*a*), where the crystal thickness increases from the lower right corner to the upper left, shows in a certain thickness region an array of small white circles whose diameter is about 1·7 Å. The values of $z$ and $\Delta f$ being unknown for these images a large number of simulations were carried out over the parameter range covering $50 \le z \le 400$ Å and $400 \le \Delta f \le 1600$ Å in considering the partial coherence as well as the perfectly coherent illumination condition. Thus, Fig. 4(*d*) and Fig. 5(*b*) were found at $z = 100$ Å with $\Delta f = 450$ and 1350 Å respectively in the coherent case, while they were completely destroyed by the partial coherence (even by the finite spatial coherence only) as shown *e.g.* in Fig. 5(*c*) which was obtained by using the intensity-sum method (see later) not only over the effective source but also over $\Delta f$. Furthermore, the diameter of the small circles in Fig. 5(*b*) is about 2·3 Å and so significantly larger than the observed one. In simulation these circles appear when $\Delta f + z$ is nearly equal to 1450 Å for $z$ ranging from 75 to 125 Å. The intensity of the 110 reflection, the most intense of all the reflections on the zone axis, has its first maximum amid the thickness region, and the partial coherence replaces circles by fringes of 2·48 Å period owing to the interference between the 110 and central beams, resulting in the image of Fig. 5(*c*) somewhat like that observable in the thicker region (upper left corner in Fig. 5*a*). A similar type of image has been obtained from a gold crystal and presents some differences from calculated images (Hashimoto *et al.*, 1978-79). At present it is not clear if, by considering the partial coherence, there is any approximation which becomes defective in certain situations of dynamical scattering in rather thick crystals. The imaging parameters being unknown it will be reasonable not to pursue further discussion on these images. It is worth noting that the image of Fig. 4(*a*) shows white dots separated by about 1·3 Å or less indicating a good stability of the microscope.

* All the defocus values appearing in the present paper designate those of underfocus.

Fig. 6(*a*)–(*d*) shows part of the focus series from a crystal oriented along the [010] zone axis and the corresponding simulations at $z = 50$ Å. The projected potential and atom positions are reproduced in Fig. 6(*e*) and (*f*), respectively. The evolution of image appearance with defocus value seen in Fig. 6(*a*), (*b*) and (*c*) is similar to that of the [2$\bar{2}$1] orientation (Fig. 3). The finest image details are visible in Fig. 6(*d*), but there is no simple correspondence with the projected structure except that the nearest-neighbor columns of vanadium atoms (separated by 1·47 Å) are not resolved and appear as a dark patch.

From these results it can be said that, at least as far as thin crystals are concerned, experimentally observed images may be reproduced by simulation if the defocus value is to be estimated from the focus setting on the microscope. In fact it is these two parameters, $z$ and $\Delta f$, that are of capital importance in image contrast and, at the same time, are difficult to determine with sufficient precision, say, the order of the defocus spread. In some favourable cases, however, lattice images can be interpreted more objectively. If there is a certain amount of contamination or an amorphous part of the crystal under observation which is not so heavy that it disturbs the lattice image, the defocus value can be measured with the technique of optical diffraction. If the crystal is in the shape of a thin wedge whose angle is neither too large nor too small to observe several equal-thickness fringes, the crystal thickness can be estimated by comparison with the theoretical profile. A case where these two conditions are nearly satisfied is presented here.

Fig. 7(*a*) shows a low-magnified bright-field image taken from a crystal in the [$\bar{4}$11] zone-axis orientation using only the central spot. The corresponding diffraction pattern is shown in Fig. 1(*f*). The microdensitometry was carried out in the direction $A$ to $A'$ on the original negative. The recorded optical density curve is reproduced in Fig. 7(*b*). In Fig. 7(*c*) are shown the corresponding theoretical profiles of the equal-thickness fringes calculated with 65 (continuous line) and 101 (dotted line) waves. It is clear that 65 waves are sufficient to describe the dynamic scattering of electrons arising in the crystal of this orientation. By comparing the theoretical and experimental $I_{000}$ curves the crystal thickness was estimated from point to point on the image shown in Fig. 7(*a*). The double-dotted curve in Fig. 7(*c*) represents the calculated intensity of the 0$\bar{1}$1 reflection which is kinematically forbidden and corresponds to a lattice spacing of 4·10 Å.

Fig. 8 shows optical diffractograms obtained from three negatives bearing lattice images of the same crystal in the same orientation that is presented in the previous figure. In the optical Fourier transformation a mask was used to select the edge region of the crystal where some contaminations were visible, and it gave rise to the streak on diffraction spots arising from the lattice image. Apart from the spots one or two annuli are also visible on the diffractograms. The value of $C_s$ being known to be 1·0 mm, the defocus value (at least, that of the edge part of the crystal) was measured from these annuli: 640 Å for (*a*), 1000 Å for (*b*) and 1210 Å for (*c*) with a possible error of about ±50 Å. The lattice images from which

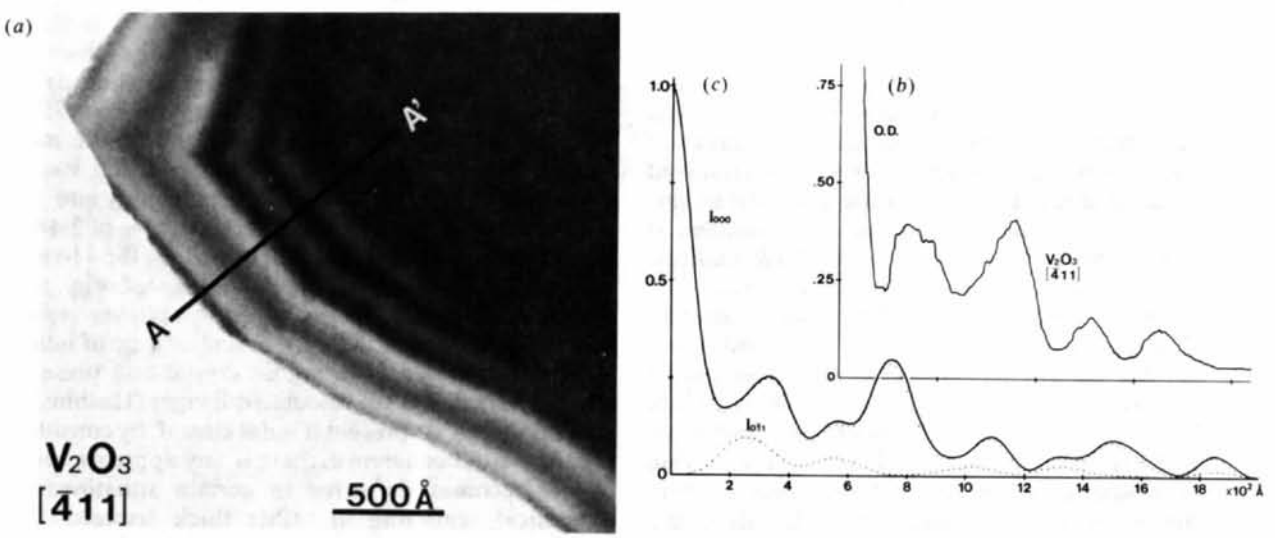


Fig. 7. (*a*) Bright-field image formed by using only the central beam from a [$\bar{4}$11] oriented crystal whose diffraction pattern is reproduced in Fig. 1(*f*). The microdensitometry was carried out on the original negative following $A$ to $A'$. The crystal thickness was estimated by comparing the resulting optical density curve (*b*) with the theoretical profile of equal-thickness fringes $I_{000}$ in (*c*) calculated with 65 waves (continuous curve) and 101 waves (dotted curve). The double-dotted curve represents the calculated intensity of equal thickness fringes for the kinematically forbidden reflection 0$\bar{1}$1.

these diffractograms were generated are reproduced in Fig. 9(*a*), (*b*) and (*c*) in the same order. The insets are the best-matched images calculated at $\Delta f = 650$ Å for (*a*), 1000 Å for (*b*) and 1150 Å for (*c*). These values are in good agreement with those found from the diffractograms. In the image simulation the defocus spread was allowed for by using the intensity-sum method (see the following section). Here, owing to Fig. 7, the crystal thickness was taken to be 50 Å for the thinnest region seen near the bottom of each image showing the amorphous contamination. The 4·10 Å periodicity due to the forbidden reflection is recognizable. By comparing the simulated images with the projected crystal structure of Fig. 9(*e*) and the potential distribution Fig. 9(*d*), one can interpret the experimental images as follows. White patches seen in the image (*b*) correspond to the regions where the projected potential is high, namely they correspond to atomic-column sites, and those in the image (*c*) correspond to tunnel sites surrounded by atomic columns, while the image (*a*) does not reflect directly the crystal structure.

### 4.2. *Validity of the envelope-function approximation*

In order to take account of the effect of the partial coherence on the lattice-image contrast a method currently employed in the image simulation is the envelope-function approximation (see, for example, Spence *et al.*, 1977). Although very convenient to incorporate in the simulation, the method is, however, subject to some theoretical conditions. It is only applicable to the object of weak contrast; in other words, it is valid only if all the interferences between diffracted beams are negligible in image contrast compared with those between the main beam and the diffracted beams. Moreover, an additional condition for the spatial coherence part is that the effective source must not be very large, *i.e.* the generalized source size $U_S = (C_s\lambda^3)^{1/4}u_s \lesssim 0{\cdot}138$ (Frank, 1973). In the case of large-unit-cell complex oxide crystals the approximation appears to be generally satisfactory to explain the observed image contrast (see, for example, § 5.8 in Spence, 1981). When a crystal of smaller unit cell is studied, however, it becomes doubtful that the above-mentioned conditions are always satisfied. Therefore, it is worth while in the case of $V_2O_3$ to compare the image calculated by use of this method with that obtained by summing the image intensity over the finite effective source (spatial coherence) and over the distribution of the defocus fluctuation (temporal coherence) (O'Keefe & Sanders, 1975; Bursill & Wilson, 1977). However, the latter, let us call it the 'intensity-sum method', naturally needs computation of very long duration if it is applied strictly as is the case for Fig. 5(*c*), which will render it impractical. So, let us examine first of all the effect of the temporal coherence alone by image simulation.

The temporal coherence is caused, for the most part, by the electronic instability of the microscope and can be treated in the image simulation in terms of the defocus fluctuation, also called the defocus spread. In order to describe this we assumed a Gaussian distribution with the standard deviation of 50 Å (Olsen & Spence, 1981). Fig. 10 shows different kinds of focus series calculated in the [$\bar{4}$11] zone-axis orientation. The crystal thickness of 150 Å was chosen because the most intense reflection 104 there attains its first peak, which is slightly higher than the first minimum of the main beam occurring almost at the

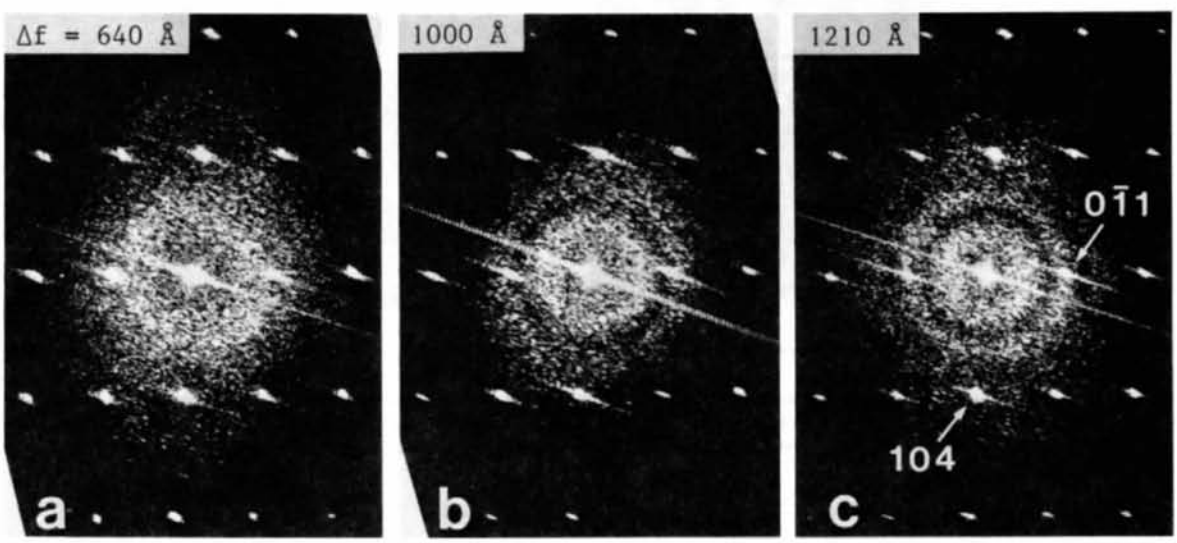


Fig. 8. Optical diffractograms obtained from [$\bar{4}$11] lattice images of the crystal shown in Fig. 7. The defocus values thus found are (*a*) 640 Å, (*b*) 1000 Å and (*c*) 1210 Å. The streak on the spots arises from the mask used in the optical Fourier transformation.

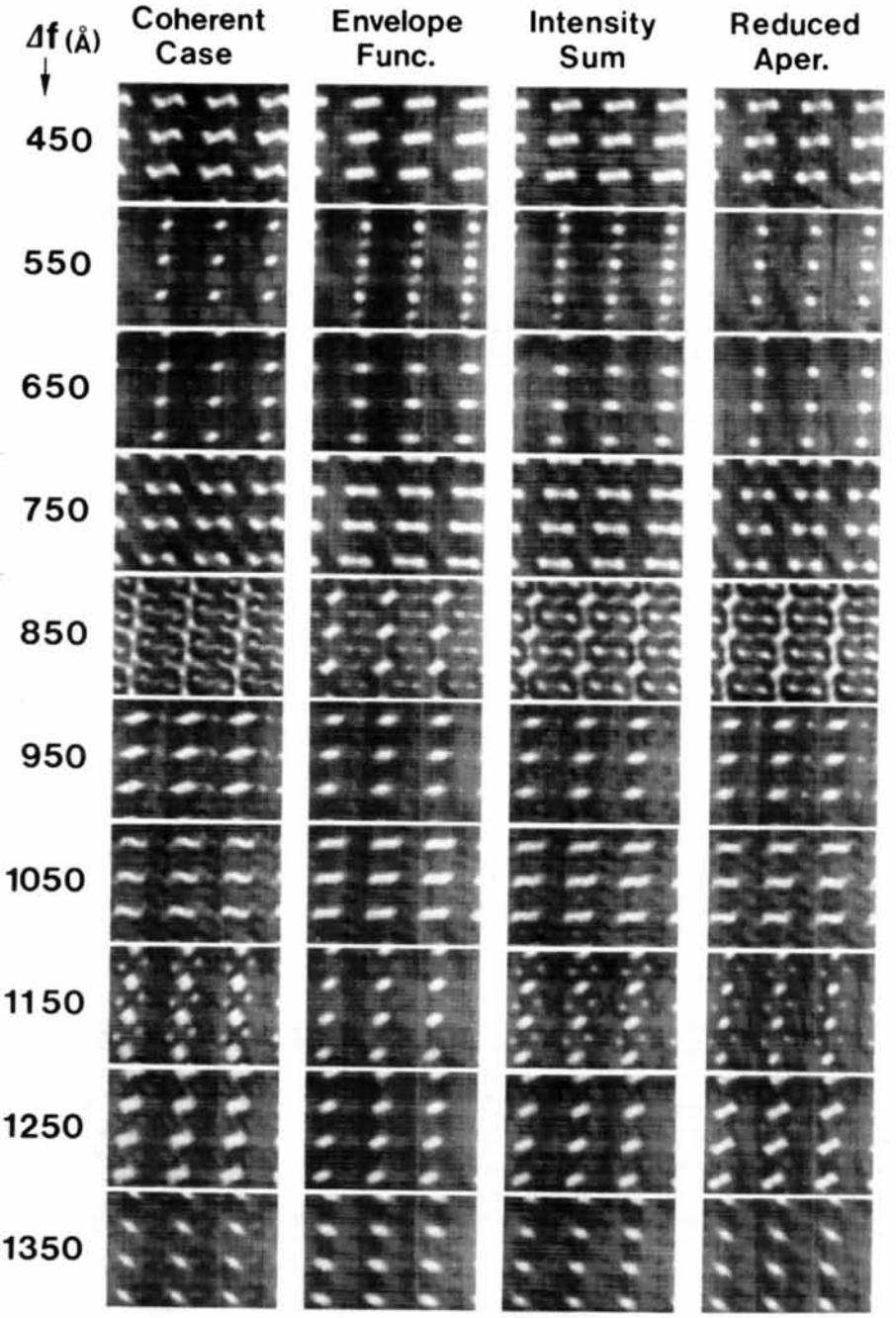


Fig. 10. Focal series calculated in [$\bar{4}11$] orientation to compare different methods allowing for the effect of the temporal coherence (defocus spread) on lattice-image contrast. The incident beam is considered to be parallel. A Gaussian distribution of the standard deviation $\sigma = 50$ Å is assumed for the defocus spread in the envelope-function approximation and the intensity-sum method (see text). Reduced aper. refers to a perfectly coherent case but with use of a reduced objective aperture $R = 0{\cdot}77$ Å$^{-1}$, while in the other three cases $R = 0{\cdot}94$ Å$^{-1}$ was used. The crystal thickness was taken to be 150 Å, as the first minimum occurs near there for the central beam intensity.

same time. To see the variation in image appearance with defocus values it was sufficient to take the defocus range to cover half of the largest Fourier-image period $2d^2/\lambda = 1340$ Å for the $01\bar{1}$ reflection. The four series are:

1st column – perfectly coherent case (for reference)
2nd column – envelope-function approximation used,
3rd column – intensity-sum method used, and
4th column – perfectly coherent case but with an objective aperture of $R = 0{\cdot}77$ Å$^{-1}$.

The objective aperture considered in the first three cases is that used in the experiments ($R = 0{\cdot}94$ Å$^{-1}$) and shown in Fig. 1(*f*), while the reduced aperture in the last case was taken from the smallest separation between two dots recorded in our experiments (*e.g.* Fig. 4*a*). The information resolution limit (Spence, 1981) due to the envelope function with a defocus spread of 50 Å gives 0·74 Å$^{-1}$, practically the same as the reduced aperture. However, it will be reasonable not to insist on the information resolution limit, a notion founded on weakly scattering objects, because it is not evident that the condition is satisfied in the case of $V_2O_3$ crystals in reality. In our case, there is no *a priori* reason to exclude a 1·3 Å period from the image formation because the dots are neither the noise nor one-dimensional fringes. Comparing these focus series one can see that the effect of the temporal coherence on the image contrast is not negligible, that there are certain defocus values such as $\Delta f = 850$ and 1150 Å where the envelope-function approximation deviates appreciably from the intensity-sum method, and that the simple reduced aperture gives a rather good approximation to what is obtained by use of the intensity-sum method.

The other component of the partial coherence, namely the spatial coherence, arises from the fact that the incident beam is not parallel, and can be described by a finite size of the effective source (Frank, 1973). This is defined, in our illumination conditions, by the size of the second-condenser aperture. The intensity-sum method for the spatial coherence consists of adding the image intensities calculated for different incident directions considered inside the cone of the convergent incident beam. This is an approximation to the integration of image intensity over the effective source. For the $[2\bar{2}1]$ and $[\bar{4}11]$ zone axes, Fig. 11 shows some images calculated as a function of the number of directions considered in the effective source of radius $u_s = 0{\cdot}030$ Å$^{-1}$. This value being small enough, the exit-surface wave field calculated for the central direction (that lying on the optical axis) was used for the other directions describing the effective source, which is an approximation also made in the envelope-function method. It is thus seen that the 17 directions are practically sufficient to represent the effective source used in the experiments.

Making use of these results from image simulations, let us now see the global effect of the partial coherence on the lattice-image contrast. In Fig. 12 is reproduced an experimental image obtained from a wedge-shaped crystal in the $[\bar{4}11]$ orientation, the figures on which indicate the crystal thickness estimated from equal-thickness fringes. First of all, a series of the best-matched images was searched by varying the defocus value ($\Delta f$) for different crystal thicknesses ($z$) by use of the intensity-sum method. For this purpose, the image intensity was summed over the 17 directions mentioned above, while the reduced aperture of $R = 0{\cdot}77$ Å$^{-1}$ was assumed to allow for the temporal coherence. Another series of images was then calculated for the same pairs of parameters ($z$, $\Delta f$) as before, but now using the envelope function with $R = 0{\cdot}94$ Å$^{-1}$ and a disk-shaped source of $u_s = 0{\cdot}030$ Å$^{-1}$. The crystal thickness used in the simulation is indicated between the two corresponding images. The defocus value taken for each thickness is shown in Fig. 13 together with the maximum and minimum image intensities resulting from each method: dots for the intensity sum and circles for the envelope function. The image contrast is lower in the latter method as a result of its lower maximum intensity. The difference is small for very thin crystals as can be understood from the basic assumption made in the envelope-function approach. There are two points to be noted here; firstly, the envelope-function approximation gives an image appearance which is

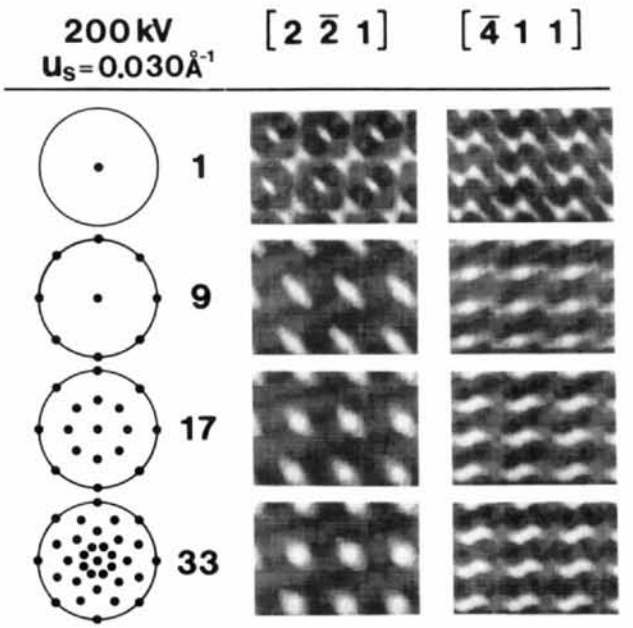


Fig. 11. Lattice images calculated by using the intensity-sum method as a function of the number of directions considered inside the cone of convergent incident beam equivalent to an effective source of radius $u_s = 0{\cdot}030$ Å$^{-1}$. The defocus spread is set to be 0 Å. The other conditions are $z = 50$ Å and $\Delta f = 450$ Å for $[2\bar{2}1]$ and 1150 Å for $[\bar{4}11]$ orientation.

very similar to that which results from the intensity-sum method in spite of the difference in intensity values and, secondly, the simulated images are in fairly good qualitative agreement with the experimental one up to a thickness of about 450 Å. In thicker regions the agreement becomes less satisfactory. Thus, a low-contrast image of network-like appearance occurring at $z = 800$ Å in simulation is experimentally visible around $z = 700$ Å.

As for the thick region ($z \gtrsim 500$ Å) of crystals, the comparison between experimental and calculated images is difficult because the contrast of the observed image is not high enough to allow the comparison of image details. In this regard, there are some problems also on the side of image simulation. The effect of the inelastic scattering is not fully considered in the calculation, which allows only for the loss of Bragg-peak intensity through phonon scattering. In other words, there is no background arising from different processes of the inelastic scattering in the calculated image, hence contributing to keep up the contrast of the latter. From a technical point of view, because of the limited darkness range (10 levels) of the grey scale used, the maximum intensity of a calculated image was always assigned the same level (the brightest of the ten), which also had a tendency to keep the apparent contrast high in simulation even for thick crystals.

## 5. Conclusions

From our study on lattice images obtained at 200 kV from $V_2O_3$ crystals one can deduce some indications useful in interpreting high-resolution images of a crystal having a relatively small unit cell ($\lesssim 5$ Å) such as semi-conductors or metals and alloys.

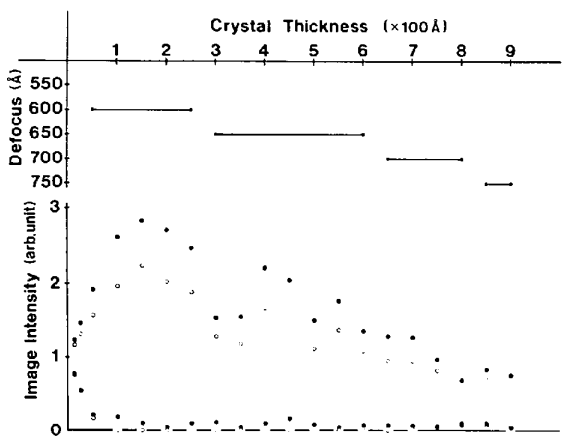


Fig. 13. Defocus values (under-focus) used in the image simulation as a function of the crystal thickness shown in Fig. 12, and the resulting maximum and minimum intensities in each image: closed and open circles stand for the intensities occurring in the intensity sum 17 and the envelope-function approximation, respectively.

As today's 100 and 200 kV high-resolution electron microscopes enable us to work under the conditions where the effect of the partial coherence on image contrast, namely that of smoothing more or less the intensity distribution in the image, is less important than it was in the past, the image contrast depends more critically upon the defocus value and the crystal thickness. It thus becomes more important for an objective interpretation of the high-resolution image to know these two imaging parameters. In some favourable cases they can be measured or estimated after a somewhat long analysis as has been shown here. Therefore it will be necessary for rapid and reliable high-resolution work to have a microscope equipped with an optical system on line with the computer in order to measure the image intensity point-by-point and to perform the Fourier transformation (Hashimoto, Takai, Yokota, Endoh & Fukada, 1980; Sinclair, Ponce, Yamashita, Smith, Camps, Freeman, Erasmus, Nixon, Smith & Catto, 1982). As regards the defocus value at the edge of a crystal under observation it will also be possible to estimate this by precisely controlling the objective-lens current of the microscope. For this purpose, however, it seems necessary to study the behavior of the Fresnel-fringe contrast on the edge of a crystal of appropriate shape in terms of the $C_s$ and defocus values without assuming a weak-phase object. This purpose is to determine the absolute defocus value when the contrast of Fresnel fringes becomes, for example, minimum on the observation screen. It should be noted that certain types of crystal defects whose structure is well known may facilitate the lattice-image interpretation (Chiang, Carter & Kohlstedt, 1980; Olsen & Spence, 1981; Ponce, Yamashita, Bube & Sinclair, 1981), and that, nevertheless, its verification by simulation or the study of defects of unknown structure cannot proceed without knowing the defocus value.

It is rather surprising that the envelope-function approximation gives results similar to those obtained by using the intensity-sum method even for relatively thick regions. This will be explained by the fact that the effect of partial coherence is not always serious enough to transform the general appearance of the image under the present experimental conditions on the one hand, and that the comparison of the two methods remains qualitative on the other.

Finally, it would be too early to think that the lattice image of a perfect crystal can now be well understood even if we exclude the effect of the inelastic scattering having increasing importance in thicker crystals. In fact we have encountered images such as those of Figs. 4 and 5 that seem difficult to reproduce by simulation. Aside from the question of partial coherence, the potential data used in image calculation is not beyond doubt. It is the lack of knowledge on the defocus and the crystal thickness that prevents further analysis of these images. An experimentally observed

evolution with crystal thickness of lattice-image contrast was reproduced rather satisfactorily by image simulation up to a crystal thickness of about 450 Å, beyond which a certain deviation appeared. The intensity profile of equal-thickness fringes used to estimate the crystal thickness was here calculated on the same potential data base that served to simulate lattice images. It will be necessary to do an independent check of the thickness in using, for example, a plane defect if there is one in the crystal. The present work furnishes an example of comparison between the observed and calculated lattice images as a function of the crystal thickness. Similar works have been reported by Rez & Krivanek (1978) on silicon, and by Ishizuka & Iijima (1981) on rutile.

We thank the Centre d'Etudes de Chimie et Métallurgique, Vitry, and the Centre d'Etudes Nucléaires, Grenoble, for having permitted us to work on their JEOL-200CX microscopes equipped for high-resolution work. One of us (MT) received a scholarship from the French Ministry of Foreign Affairs.

### References

ANDRIANOV, G. O. & DRICHKO, I. L. (1976). *Sov. Phys. Solid State*, **18**, 803–804.
BURSILL, L. A. (1978-79). *Chem. Scr.* **14**, 83–97.
BURSILL, L. A. & WILSON, A. R. (1977). *Acta Cryst.* A**33**, 672–676.
CHIANG, S. W., CARTER, C. B. & KOHLSTEDT, D. L. (1980). *Philos. Mag. A*, **42**, 103–121.
COWLEY, J. M. & IIJIMA, S. (1972). *Z. Naturforsch. Teil A*, **27**, 445–451.
FEJES, P. L. (1977). *Acta Cryst.* A**33**, 109–113.
FRANK, J. (1973). *Optik (Stuttgart)*, **38**, 519–536.
HALL, C. R. & HIRSCH, P. B. (1965). *Proc. R. Soc. London Ser. A*, **286**, 158–177.
HASHIMOTO, H., ENDOH, H., TAKAI, Y., TOMIOKA, H. & YOKOTA, Y. (1978-79). *Chem. Scr.* **14**, 23–31.
HASHIMOTO, H., TAKAI, Y., YOKOTA, Y., ENDOH, H. & FUKADA, E. (1980). *Jpn. J. Appl. Phys.* **19**, L1–4.
HIRSCH, P. B., HOWIE, A., NICHOLSON, R. B., PASHLEY, D. W. & WHELAN, M. J. (1965). *Electron Microscopy of Thin Crystals.* London: Butterworths.
IIJIMA, S. (1971). *J. Appl. Phys.* **42**, 5891–5893.
ISHIZUKA, K. & IIJIMA, S. (1981). *39th Ann. Proc. EMSA*, edited by G. W. BAILEY, pp. 96–97. Baton Rouge: Claitor.
KRAKOW, W. (1979). *Ultramicroscopy*, **4**, 55–76.
KRIVANEK, O. L. (1976). *Optik (Stuttgart)*, **45**, 97–101.
KRIVANEK, O. L. & REZ, P. (1980). *38th Ann. Proc. EMSA*, edited by G. W. BAILEY, pp. 170–171. Baton Rouge: Claitor.
LAUNAY, J. C. (1977). *Contribution à l'Etude du Transport en Phase Vapeur de Quelques Oxydes d'Eléments de Transition.* Thèse Univ. de Bordeaux I.
LAUNAY, J. C., POUCHARD, M., AYROLES, R. & JOUFFREY, B. (1975). *Mater. Res. Bull.* **10**, 559–564.
O'KEEFE, M. A. & IIJIMA, S. (1978). *Proc. Ninth International Congress on Electron Microscopy, Toronto*, Vol. I, pp. 282–283.
O'KEEFE, M. A. & SANDERS, J. V. (1975). *Acta Cryst.* A**31**, 307–310.
OLSEN, A. & SPENCE, J. C. H. (1981). *Philos. Mag. A*, **43**, 945–965.
PONCE, F. A., YAMASHITA, T., BUBE, R. H. & SINCLAIR, R. (1981). *Defects in Semiconductors*, edited by J. NARAYAN & T. Y. TAN, pp. 503–508. New York: North-Holland.
RADI, G. (1970). *Acta Cryst.* A**26**, 41–56.
REZ, P. & KRIVANEK, O. L. (1978). *Proc. Ninth International Congress on Electron Microscopy, Toronto*, Vol. I, pp. 288–289.
SCHERZER, O. (1949). *J. Appl. Phys.* **20**, 20–29.
SINCLAIR, R., PONCE, F. A., YAMASHITA, T., SMITH, D. J., CAMPS, R. A., FREEMAN, L. A., ERASMUS, S. J., NIXON, W. C., SMITH, K. C. A. & CATTO, C. J. D. (1982). *Nature (London)*, **298**, 127–131.
SPENCE, J. C. H. (1981). *Experimental High-Resolution Electron Microscopy.* Oxford: Clarendon Press.
SPENCE, J. C. H., O'KEEFE, M. A. & KOLAR, H. (1977). *Optik (Stuttgart)*, **49**, 307–323.
TANAKA, M. & JOUFFREY, B. (1980). *Acta Cryst.* A**36**, 1033–1041.
TANAKA, M. & JOUFFREY, B. (1981). *J. Microsc. Spectrosc. Electron.* **6**, 6a.
WADE, R. H. & FRANK, J. (1977). *Optik (Stuttgart)*, **49**, 81–92.